Article

peri-Fused polyaromatic molecular contacts for perovskite solar cells

https://doi.org/10.1038/s41586-024-07712-6

Received: 29 November 2023

Accepted: 12 June 2024

Ke Zhao[1,2,11], Qingqing Liu[2,11], Libing Yao[2,11], Caner Değer[3], Jiahui Shen[1,4], Xu Zhang[1,2], Pengju Shi[1,2], Yuan Tian[1,2], Yixin Luo[1], Jiazhe Xu[1,2], Jingjing Zhou[1,2], Donger Jin[1], Sisi Wang[2], Wei Fan[1,2], Shaochen Zhang[1,2], Shenglong Chu[2], Xiaonan Wang[1,2], Liuwen Tian[1,2], Ruzhang Liu[4], Li Zhang[5], Ilhan Yavuz[3], Hong-fei Wang[5], Deren Yang[1], Rui Wang[2,6,7,8] ✉ & Jingjing Xue[1,9,10] ✉

Molecule-based selective contacts have become a crucial component to ensure high-efficiency inverted perovskite solar cells[1–5]. These molecules always consist of a conjugated core with heteroatom substitution to render the desirable carrier-transport capability[6–9]. So far, the design of successful conjugation cores has been limited to two N-substituted π-conjugated structures, carbazole and triphenylamine, with molecular optimization evolving around their derivatives[2,5,10–12]. However, further improvement of the device longevity has been hampered by the concomitant limitations of the molecular stability induced by such heteroatom-substituted structures[13,14]. A more robust molecular contact without sacrificing the electronic properties is in urgent demand, but remains a challenge. Here we report a *peri*-fused polyaromatic core structure without heteroatom substitution that yields superior carrier transport and selectivity over conventional heteroatom-substituted core structures. This core structure produced a relatively chemically inert and structurally rigid molecular contact, which considerably improved the performance of perovskite solar cells in terms of both efficiency and durability. The champion device showed an efficiency up to 26.1% with greatly improved longevity under different accelerated-ageing tests.

Inverted perovskite solar cells (PSCs) are superior in device durability, compatibility with tandem structures and thus market-integration potentials, compared with their normal counterparts[10,15–19]. The research on inverted PSCs has recently gained impetus with the advent of molecule-based hole-selective contacts, which has boosted the device power conversion efficiencies (PCEs)[1–5]. These molecules, featuring conjugated moieties, can usually self-assemble into monolayers or multiple layers at the interface of transparent electrodes and perovskites to ensure efficient charge transport[20–22]. Their unique set of traits, such as ease of fabrication, minimized parasitic absorption and structural tunability, has made them outperform conventional selective contacts and become indispensable in achieving high-efficiency inverted PSCs[6,23,24].

The molecular design of such selective contacts always involves π-conjugated hydrocarbon structures with heteroatom substitution[6]. The introduction of heteroatoms, such as N, S and O, to the conjugation core is generally thought to deliver enriched electron density originating from lonely-electron delocalization, which ensures an efficient charge-transport capability[7–9]. The most successful conjugation cores of the molecular contacts used in inverted PSCs are carbazole and triphenylamine (and their derivatives), both of which are N-substituted heterocyclic structures[2,5,10]. Extensive research on the structural optimization of the molecules, such as side-chain engineering, heteroatom insertion and functional-group tailoring, has thereby evolved around these two backbones[10–12]. However, the heteroatom-substituted structures often promise desirable electronic properties but with reduced structural integrity[13,14]. Upon heteroatom substitution, reactive sites can be concomitantly introduced owing to the polarized chemical bonds, leading to potential structural instability, particularly under external fields such as bias and illumination[9,24,25]. More inert conjugation cores for molecular contacts while maintaining high electronic performance is essential to the long-term stability of PSCs, which is the major obstacle towards their commercialization, but has yet to be discovered.

Here we report a molecular structure, (2-(pyren-1-yl)ethyl)phosphonic acid, named Py3, for constructing a robust molecular contact. Different from all the reported molecules for selective contacts so far (Extended Data Fig. 1), Py3 features a conjugation core of pyrene without any heteroatom substitution while expressing exceptional electronic properties at the interface. Its *peri*-fused polyaromatic structure is chemically inert and conformationally rigid, allowing for a secured molecular interface for efficient charge extraction. In-depth

---

[1] State Key Laboratory of Silicon and Advanced Semiconductor Materials and School of Materials Science and Engineering, Zhejiang University, Hangzhou, China. [2] School of Engineering, Westlake University and Institute of Advanced Technology, Westlake Institute for Advanced Study, Hangzhou, China. [3] Department of Physics, Marmara University, Istanbul, Turkey. [4] School of Chemistry and Chemical Engineering, Yangzhou University, Yangzhou, China. [5] School of Science, Westlake University, Hangzhou, China. [6] Division of Solar Energy Conversion and Catalysis at Westlake University, Zhejiang Baima Lake Laboratory Co. Ltd, Hangzhou, China. [7] Research Center for Industries of the Future, Westlake University, Hangzhou, China. [8] Zhejiang Provincial Key Laboratory of Intelligent Low-Carbon Biosynthesis, Westlake University, Hangzhou, China. [9] Shanxi-Zheda Institute of Advanced Materials and Chemical Engineering, Taiyuan, China. [10] Shangyu Institute of Semiconductor Materials, Shaoxing, China. [11] These authors contributed equally: Ke Zhao, Qingqing Liu, Libing Yao. ✉e-mail: wangrui@westlake.edu.cn; jjxue@zju.edu.cn

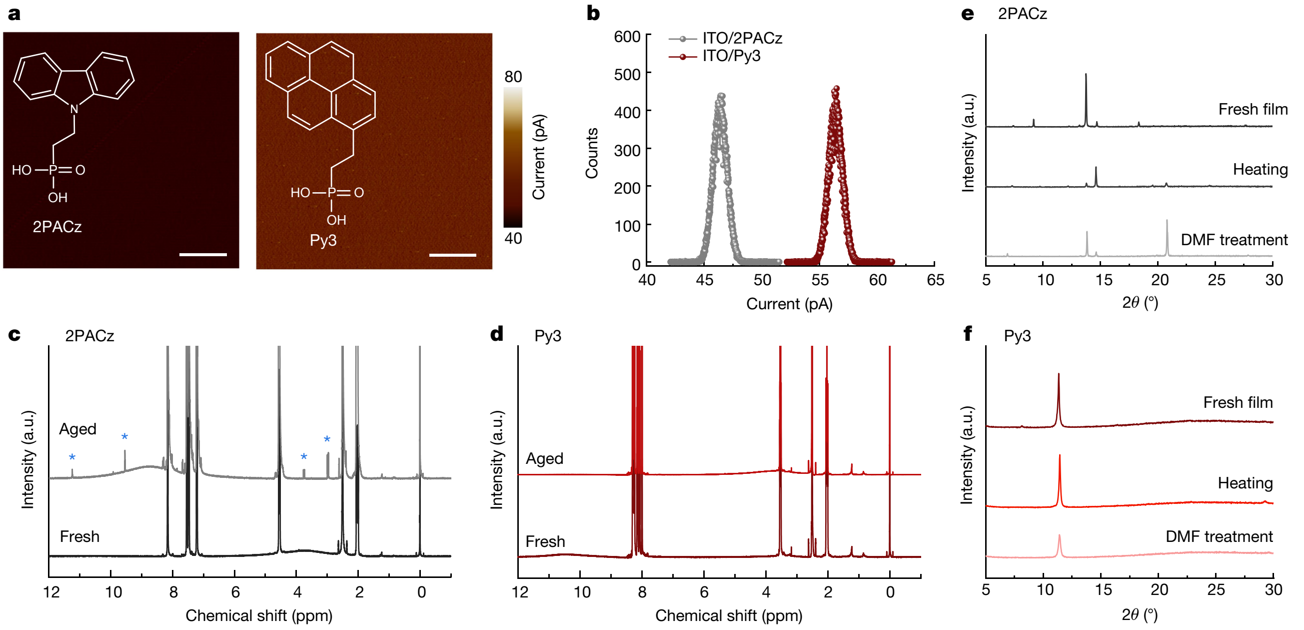

Fig. 1 | Basic properties of assembled Py3 as molecular contacts for PSCs. **a**,**b**, c-AFM images (**a**) and the corresponding surface current signals (**b**) of the ITO substrate covered with 2PACz and with Py3. Scale bars, 2 μm. **c**,**d**, NMR spectra of 2PACz (**c**) and Py3 (**d**) before and after illumination. The blue asterisks denote the new NMR peaks that emerge. **e**,**f**, XRD patterns of 2PACz (**e**) and Py3 (**f**) films before and after ageing tests of thermal annealing and organic solvent treatment.

temperature-dependent spectroscopy investigations reveal considerably strengthened intermolecular stacking and suppressed anharmonic interaction in Py3, which contributes to the improved performance of the molecular contacts. The inverted PSC constructed with Py3 achieves a PCE of 26.1%. The targeted devices show a projected T90 (the time for a solar cell to degrade to 90% of its initial efficiency) of over 10,000 h in different accelerated-ageing tests, demonstrating their greatly improved resistance to external stimuli.

peri-Fused polyaromatic structure

Extensively *peri*-fused polycyclic aromatic hydrocarbons are seen as nanographenes, embracing both high structural stiffness and desirable electronic properties for carrier transport[7,9]. Motivated by this combination, we designed a pyrene structure, the smallest *peri*-fused polyaromatic system, to replace the frequently used conjugation core in the (2-(9H-carbazol-9-yl)ethyl)phosphonic acid (2PACz) or triphenylamine series. The as-synthesized Py3 molecule showed good solubility and can be easily solution-processed (see synthesis details in Supplementary Text 1). Upon deposition onto the indium tin oxide (ITO) glass substrate, as for the frequently used 2PACz, Py3 delivered a uniform surface coverage. The conductive atomic force microscopy (c-AFM) images of the ITO substrate covered with 2PACz and with Py3 are compared in Fig. 1a. Although both 2PACz and Py3 led to homogeneous surface electronic properties, Py3 showed a higher average surface current signal of about 57 pA compared with 2PACz (about 46 pA; Fig. 1b). The higher conductivity revealed by c-AFM suggested enhanced charge transport, thus idicating that Py3 is a promising molecular contact for facilitated charge flow, despite the absence of heteroatom doping to enrich the electron density. The improved charge-transport capability could arise from the extended π-conjugation and the enhanced conformational rigidity of Py3, which encourages electron delocalization.

Owing to the all-carbon based aromatic backbone, Py3 was expected to better maintain its molecular integrity under external stimulus. We used nuclear magnetic resonance (NMR) spectroscopy to compare the molecular stability of 2PACz and Py3. Both molecules were aged under continuous illumination for 120 h under ambient conditions. As shown in Fig. 1c, different NMR peaks emerged in the sample of 2PACz after the ageing test, indicating the degradation of 2PACz and the formation of new chemical species. Different peaks emerged in both the alkyl (2.0–4.0 ppm) and aromatic (7.0–12.5 ppm) regions for 2PACz after the ageing test, suggesting that the polarized C–N bond in 2PACz underwent N-dealkylation, leading to the formation of carbazole and vinyl phosphonate. The formed vinyl phosphonate underwent further reactions, ultimately resulting in the formation of aldehyde- and carboxyl-bearing products (see Supplementary Fig. 1 for detailed peak assignments and degradation pathways). In contrast, the NMR spectra of Py3 remained almost identical before and after the ageing test (Fig. 1d), verifying its considerably reduced chemical reactivity. We also tested the stability of two widely used 2PACz derivatives, MeO-2PACz and Me-4PACz. The results of the NMR and ultraviolet–visible absorption spectroscopy indicate that the MeO-2PACz and Me-4PACz are even more unstable than the unsubstituted 2PACz, and that their degradation started at the substitution site (Supplementary Figs. 2–5).

In addition to the inherent stability of the molecules, we evaluated their structural robustness when they are assembled into thin films. The conjugation core always induced π–π stacking of molecules, providing them with the capability to self-assemble into periodic structures. X-ray diffraction (XRD) measurements revealed well-defined diffraction patterns in both the 2PACz and the Py3 thin films, evidencing their long-range ordered π–π assembly. The main diffraction peak of the fresh 2PACz thin film located at 13.8° was accompanied by weak diffraction patterns centred at 9.2°, 14.6° and 18.4°, suggesting multiple molecular stacking modes. Upon heating, the diffraction patterns of 2PACz greatly shifted, showing a dominant peak at 14.6° with its original main peaks diminished (Fig. 1e). This evidenced the changed π–π stacking configuration of the 2PACz molecules, suggesting unstable stacking modes under external thermal stress. In contrast, a single diffraction peak appeared in the fresh Py3 film, which remained almost invariant after heating, implying a strong and dominant stacking mode in Py3 (Fig. 1f). As the perovskite layer was subsequently deposited onto these molecular layers for device construction, we further tested their resistance to dimethylformamide (DMF), the frequently used organic solvent for perovskite-layer deposition. Similar to the thermal test,

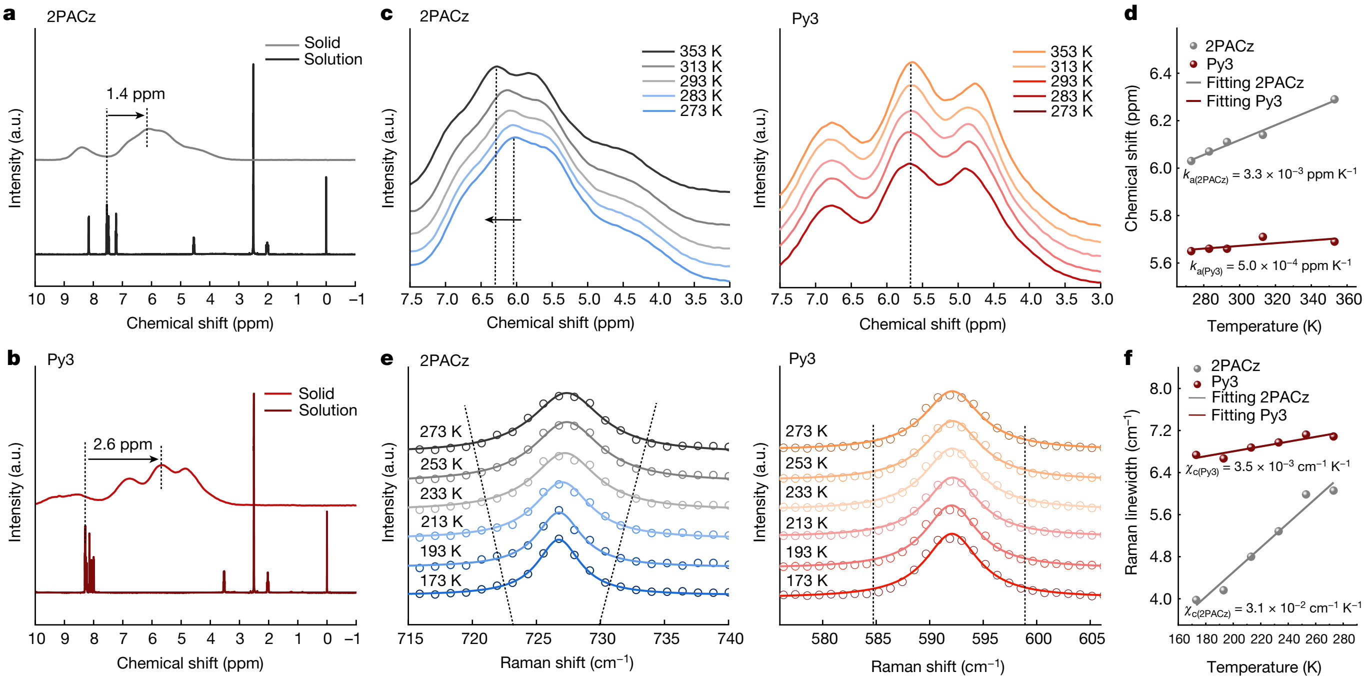

Fig. 2 | Mechanistic investigations on the molecular stacking and structural rigidity of Py3. a,**b**, Comparison of the solution-state and solid-state NMR spectra of 2PACz (**a**) and Py3 (**b**). **c**, Temperature-dependent solid-state NMR spectra of 2PACz (left) and Py3 (right). **d**, The change of chemical shift as a function of temperature for 2PACz and Py3. **e**, Temperature-dependent Raman spectra of 2PACz (left) and Py3 (right). **f**, The change of Raman linewidth as a function of temperature for 2PACz and Py3.

the XRD peak position of Py3 remained at 11.4° after DMF treatment, whereas different diffraction patterns emerged in the 2PACz film, suggesting its structure distortion upon DMF treatment (Fig. 1e,f). The improved resistance to DMF in the Py3 film could help minimize structural deformation at the interface during the perovskite-film deposition. This would benefit the interfacial contact between the molecules and perovskites to suppress the non-radiative carrier recombination.

Molecular packing and structure rigidity

To gain mechanistic insights into the improved structural rigidity of Py3, we performed molecular-level analysis on the assembled thin films. As revealed by solid-state nuclear magnetic resonance (ssNMR) spectroscopy, the aromatic signals in the ^{1}H NMR spectra of 2PACz were located at 6.1 ppm, which appeared upfield by 1.4 ppm relative to those in their solution-state spectra[26,27] (Fig. 2a). The discrepancy in the chemical shift between the solution- and solid-state 2PACz was correlated to the molecular aggregation. In the solid state, the self-assembly of the molecules is driven by the intermolecular π–π stacking, leading to a shielding effect on the aromatic protons. For Py3, such chemical shift variation increased to 2.6 ppm, suggesting a more pronounced shielding effect (Fig. 2b). This implies that Py3 features a stronger π–π interaction within the conjugation core, which results in the enhanced rigidity of its self-assembled molecular framework. The stronger π–π interaction can be attributed to the high planarity of the pyrene core owing to the absence of heteroatoms.

The enhanced molecular stacking caused by the strong π–π interaction was further verified by the temperature-dependent ssNMR measurements. As the temperature increased from 273 K to 353 K, the resonance peaks of the aromatic protons in 2PACz showed gradual downfield shifts (Fig. 2c). As an elevated temperature could weaken the π–π interaction, the aromatic protons would become less shielded by their neighbouring molecules. Therefore, the temperature dependency of the downfield resonance reflected the π–π interaction energy of the conjugation core[28,29]. Figure 2d shows the chemical-shift variation of the aromatic protons as a function of the temperature. The chemical shift increased approximately in a linear manner with increasing temperature, the slope of which we defined as an association coefficient of stacked molecules (k_a). The association coefficient k_a can be seen as a factor that is inversely proportional to the π–π interaction energy of the conjugation core. The k_a value of 2PACz was thus determined to be 3.3×10^{-3} ppm K^{-1}. For the Py3, however, the peak positions of its low-field resonances were almost unchanged as the temperature varied (Fig. 2c). The linear fitting of the chemical-shift variation with temperature verified a fairly small k_a value of 5.0×10^{-4} ppm K^{-1}, which was nearly an order of magnitude lower than that of 2PACz. The π–π interaction energy of the pyrene core in Py3 was thereby proved to be much higher than that of 2PACz, which led to its considerably strengthened molecular build-up.

Temperature-dependent Raman spectroscopy was utilized for investigating the vibrational dynamics of the assembled molecules. The ring breathing modes located at around 727 cm^{-1} for 2PACz and 592 cm^{-1} for Py3 are magnified for comparison (Fig. 2e). As the temperature increased from 173 K to 273 K, peak broadening was observed in 2PACz. This was attributed to the anharmonic couplings between the vibrons and phonons, which became thermally populated as the temperature rose[30–32]. The linewidths of the scattering patterns as a function of temperature are plotted in Fig. 2f. All the linewidths given are full-width at half-maximum for Lorentzian line shapes. The temperature-dependent Raman linewidth plot was simplified by a first-order linear approximation, the slope of which denoted a coupling coefficient χ_c. For 2PACz, the value of χ_c was calculated to be 3.1×10^{-2} cm^{-1} K^{-1}. In contrast, the ring breathing mode of Py3 showed negligible peak broadening with temperature (χ_c was 3.5×10^{-3} cm^{-1} K^{-1}), implying suppressed anharmonic interactions that stemmed from enhanced molecular rigidity. The Raman bands below 200 cm^{-1} depicted the vibrational dynamics of the most delocalized low-frequency phonons, which better described the ensemble behaviour of the assembled molecules. Similar to the intramolecular ring breathing mode, the linewidth of the phonon mode in 2PACz was highly temperature dependent, whereas the linewidth of

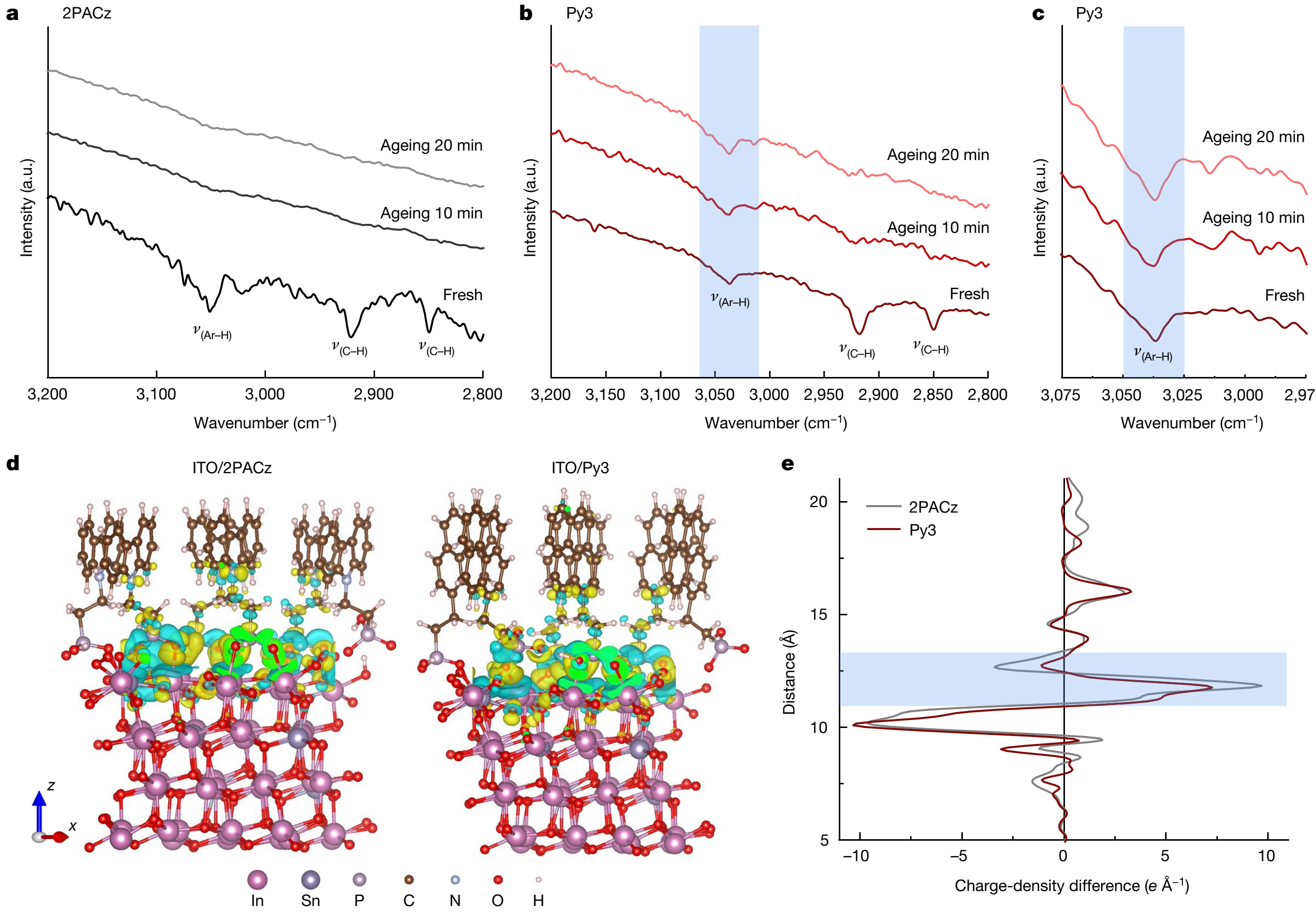

Fig. 3 | Stacking orientation and the resulting charge-carrier behaviours. **a**,**b**, Polarized FTIR spectra measured with p-polarization for the fresh and aged films of 2PACz (**a**) and Py3 (**b**). **c**, Magnification of the aromatic C–H stretching bands of Py3 at different ageing states. The blue bands denote the vibration bands of aromatic C–H stretching. **d**, Theoretical models of 2PACz and Py3 assembled on the ITO surface. **e**, Calculated charge-density difference along the vertical direction to the ITO surface. The blue band denotes the interface between the molecular layer and the perovskite layer.

Py3 was almost unchanged with temperature (Extended Data Fig. 2). The suppressed phonon coupling would also benefit the charge transport across the molecular contacts, contributing to the improved electronic properties.

As the carrier-transport behaviour is governed by the stacking orientation of the molecules, we performed polarized Fourier-transform infrared (FTIR) spectroscopy to reveal the molecular stacking geometries. 2PACz showed a typical aromatic C–H stretching vibration mode at 3,051 cm^{-1} with p-polarization, indicating that the conjugation core has a perpendicular component with respect to the substrates (Fig. 3a). Vibration bands at 2,920 cm^{-1} and 2,849 cm^{-1}, which can be attributed to the C–H stretching in the tethering alkyl chain, were also observed with p-polarization. The probed bonds perpendicular to the substrate suggested the vertical orientation of 2PACz with its conjugation tail of carbazole stacking in an in-plane ordering manner and the anchoring group of phosphonic acid binding to the ITO surface[4,12]. The interaction of the anchoring group with the ITO surface was confirmed by the peak shifts of In 3*d* and Sn 3*d* in the X-ray photoelectron spectroscopy measurements (Supplementary Fig. 6). This molecular stacking conformation was found to be disrupted upon thermal ageing. After heating the 2PACz film to 130 °C for 10 min and 20 min, all the vibration bands detected in the fresh sample with p-polarization vanished, which suggested a transformed molecular orientation from the vertical to the parallel direction. The observed change in the molecular stacking was consistent with the XRD measurements above revealing different diffraction patterns before and after thermal annealing of the film.

The Py3 film was found to hold a similar molecular orientation to the 2PACz film in its fresh state, but stand in sharp contrast to 2PACz when heated. When probed with p-polarization, the Py3 sample showed the aromatic C–H stretching band at 3,037 cm^{-1}, and the alkyl C–H stretching bands at 2,919 cm^{-1} and 2,849 cm^{-1} (Fig. 3b). After the thermal ageing test at 130 °C for 10 min and 20 min, the signals from the alkyl C–H stretching vibration reduced, suggesting deviated orientation of the tethering alkyl chain from the vertical direction. However, the vibration peak from the aromatic C–H stretching remained almost invariant during the thermal ageing, signifying the undistorted orientation of the conjugation tail of pyrene in Py3 (Fig. 3c). Therefore, although the thermally activated chain motion altered the conformation of the tethering group, the pyrene core was unaffected and served as a lock to maintain the general orientation of the molecular stacking. This in turned verified that the structural rigidity was afforded by the *peri*-fused polyaromatic structure, which featured strong π–π interaction. As the electrons are delocalized in the conjugation plane, the maintained perpendicular orientation of the conjugation unit was crucial to ensure efficient carrier transport across the interface. We used density functional theory calculations to investigate the charge distribution at the interface between the ITO substrate and the molecules. An ordered monomolecular layer was put on the surface of the ITO, disregarding the layers atop to better reflect the interfacial structures, which was confirmed by the sum-frequency-generation vibrational spectroscopy (see detailed results and discussions in Supplementary Text 2). Geometry optimization results of the ITO surface bonded to 2PACz and to Py3 are depicted in Fig. 3d, demonstrating a vertical orientation of the

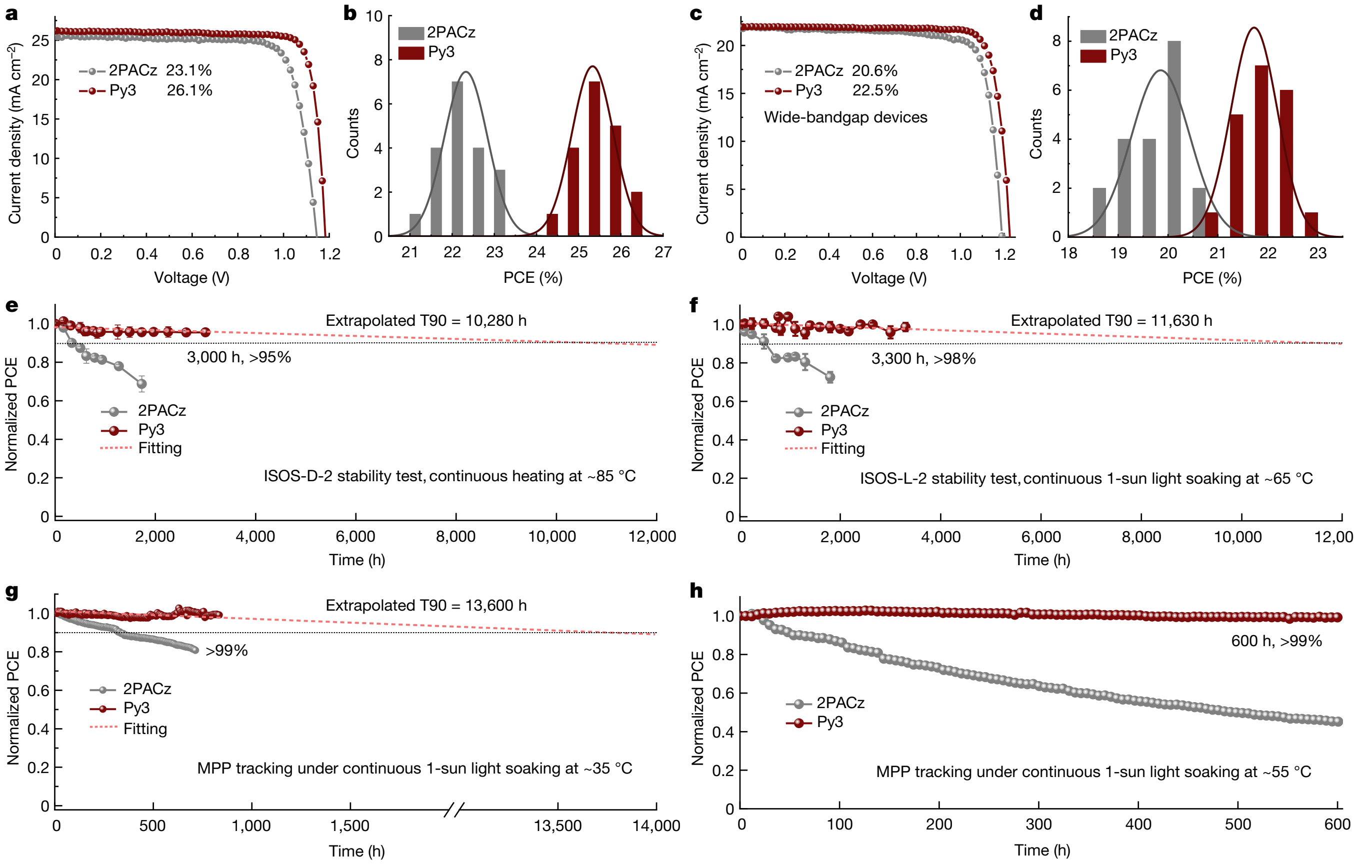

Fig. 4 | Photovoltaic performance of PSCs. a, *J*–*V* curves of the champion PSCs based on 2PACz and Py3. **b**, The statistics of the PCE values obtained from the *J*–*V* characteristics for PSCs with 2PACz and Py3. **c**, *J*–*V* curves of the champion PSCs with wide-bandgap perovskite absorbers using 2PACz and Py3. **d**, The statistics of the PCE values for the wide-bandgap PSCs. The histograms show the device efficiencies of 20 cells per type, fitted with Gaussian distributions (solid lines). **e**, Evolution of the PCEs tracked under continuous heating at about 85 °C following the ISOS-D-2 protocol. Error bars represent the standard deviation of five devices for each condition. **f**, Evolution of the PCEs tracked under continuous 1-sun light soaking at about 65 °C under open-circuit conditions following the ISOS-L-2 protocol. Error bars represent the standard deviation of five devices for each condition. **g**,**h**, Maximum power point (MPP) tracking of the PSCs under continuous 1-sun light soaking at about 35 °C (**g**) and at about 55 °C (**h**).

molecules, which was consistent with the polarized FTIR results. The corresponding charge-density differences along the *z* axis, which was perpendicular to the ITO surface, were derived for comparison (Fig. 3e). Both 2PACz and Py3 showed charge delocalization along the *z* axis. Noticeably, the charge-density profiles were sharpened at the contact between 2PACz and ITO (marked by the blue band), indicating charge accumulation at the interface. In comparison, the sharpening for Py3 was less pronounced. The flattened landscape supported the enhanced electron delocalization in Py3, which could facilitate carrier transport at the interface. We measured the time-resolved photoluminescence under different laser power intensities and derived the differential lifetime as shown in Extended Data Fig. 3 to delineate the interfacial carrier dynamics. At a relatively low laser fluence, the first interval at short time for Py3 was shorter than that for 2PACz, verifying improved charge extraction in Py3 compared with 2PACz.

Photovoltaic performances

Further assessment of the photovoltaic performance of the PSC devices using Py3 as the selective contact was performed, with 2PACz investigated in parallel for comparison. The PSCs were fabricated with an inverted device architecture of ITO/2PACz or Py3/$(\mathrm{FA}_{0.98}\mathrm{MA}_{0.02})_{0.95}\mathrm{Cs}_{0.05}\mathrm{Pb}(\mathrm{I}_{0.98}\mathrm{Br}_{0.02})_3$/LiF/$\mathrm{C}_{60}$/BCP/Ag (where FA is formamidinium, MA is methylammonium and BCP is 2,9-dimethyl-4,7-diphenyl-1,10-phenanthroline). The best-performing 2PACz-based device showed a PCE of 23.1%, with an open-circuit voltage (V_{OC}) of 1.14 V, a short-circuit current (J_{SC}) of 25.3 mA cm^{-2} and a fill factor of 80.0% (Fig. 4a). Replacing the conventional 2PACz layer with Py3 yielded a considerably improved PCE up to 26.1% (certified 25.7%; see the certificate in Supplementary Fig. 7) at a reverse scan with a stabilized PCE of 25.9% (Supplementary Fig. 8). The champion device showed a V_{OC} of 1.18 V, a J_{SC} of 26.0 mA cm^{-2} and a fill factor of 85.1%. The histogram of PCEs for 20 devices shown in Fig. 4b confirmed good reproducibility of the PCE improvement with Py3 (11.4% improvement in an average PCE from 22.8 ± 0.6% to 25.4 ± 0.9%). We attributed the increase in PCE to the improved interfacial carrier transport arising from promoted electron delocalization and structural rigidity that suppressed the interfacial phonon scattering. A desirable band alignment with perovskite and the electron-blocking capability of Py3, as revealed by ultraviolet photoelectron spectroscopy (Supplementary Figs. 9 and 10), also suppressed the charge-carrier combination at the interface. A slower transient photovoltage decay and a faster transient photocurrent decay for Py3-based devices corroborated the reduced carrier recombination and facilitated carrier transport at the interface (Extended Data Fig. 4).

We extended the application of Py3 to other types of PSC device to demonstrate its universal effectiveness. We fabricated PSCs with a wide-bandgap perovskite absorber ($\mathrm{Cs}_{0.05}\mathrm{MA}_{0.15}\mathrm{FA}_{0.8}\mathrm{PbI}_{2.25}\mathrm{Br}_{0.75}$), which is a critical subcell for tandem devices. The current density–voltage (*J*–*V*) curves of the best-performing wide-bandgap devices based on Py3 and 2PACz are compared in Fig. 4c. The use of Py3 yielded a PCE of 22.8% (certified 22.7%; see details in Supplementary Fig. 11), surpassing that of the 2PACz-based device (a PCE of only 20.6%). The statistical comparison of the PCEs obtained from 20 devices for each condition is shown in Fig. 4d, demonstrating an average PCE of 19.8% and 21.6% for 2PACz and Py3, respectively. The performance of Py3 was further evaluated in large-area devices to assess its scale-up potential. The good solubility and the pyrene-facilitated self-assembly capability favoured the spreading of Py3 on the ITO surface, which promised its scalability. As shown in Extended Data Fig. 5, the champion 1-cm^2 PSC device had a PCE of 23.5% with a V_{OC} of 1.14 V, a J_{SC} of 25.0 mA cm^{-2} and a fill factor of 82.9%, outperforming the 2PACz-based device (a PCE of 19.6% with a V_{OC} of 1.04 eV, a J_{SC} of 24.8 mA cm^{-2} and a fill factor of 75.9%). Extended Data Fig. 6 summarizes the statistical distribution of PCEs for the 1-cm^2 PSC device. The average PCE was increased by Py3 from 18.8% to 22.7% with improved reproducibility.

The changes in PCEs of the PSC devices were tracked over time under accelerated-ageing conditions according to the International Summit on Organic Photovoltaic Stability (ISOS) protocols. To test the thermal stability, the devices were continuously heated at 85 °C following the ISOS-D-2 protocol. While the PCE of the 2PACz-based device dropped swiftly over time, the Py3-based device retained over 95% of its initial PCE after 3,000 h, with a linear extrapolation to a T90 of 10,280 h (Fig. 4e; T90 is the time for a PSC to degrade to 90% of its maximum PCE). The significantly improved heat resistance can be ascribed to the structural rigidity of Py3 stacking, which served as a robust molecular lock at the interface. The relatively inert pyrene core of Py3 also promised the operational stability of PSCs under illumination. We aged the devices under continuous 1-sun light soaking at 65 °C under open-circuit conditions following the ISOS-L-2 protocol. The device with Py3 retained over 98% of its maximum PCE after 3,300 h with a linear extrapolation to a T90 of 11,630 h (Fig. 4f).

When tracked under the maximum power point, the device with Py3 showed minimal changes in PCE, retaining over 99.5% of its maximum PCE after about 850 h with a linear extrapolation to a T90 of 13,600 h (Fig. 4g). We also performed maximum-power-point tracking under an elevated temperature of 55 °C for the 2PACz- and Py3-based devices. The device with 2PACz retained only 45% of its maximum PCE, whereas the device with Py3 retained over 99% of its initial PCE after over 600 h (Fig. 4h) with a linear extrapolation to a T90 of 7,462 h (Supplementary Fig. 12). These stability results substantially surpassed the devices with 2PACz. This level of heat and light resistance is among the best for reported PSC devices, highlighting the significant role of Py3 in achieving PSCs with long-term stability.

Discussion

We report a *peri*-fused polyaromatic structure as an alternative to the frequently used heteroatom-substituted conjugation cores for constructing molecule-based selective contacts in PSCs. The extensive electron delocalization in combination with the high structural rigidity of the assembled molecular contact reconciled the charge-transport efficiency with the structural durability, a long-standing issue limiting the longevity of PSCs. We believe that this formulation will greatly expand the molecular reservoir for the design of selective contacts in PSCs and other molecular electronics, and encourage research beyond the heteroatom-substitution convention. The chemical and structural reliability of such a molecular design is anticipated to contribute towards the commercialization of PSCs.

Online content

Any methods, additional references, Nature Portfolio reporting summaries, source data, extended data, supplementary information, acknowledgements, peer review information; details of author contributions and competing interests; and statements of data and code availability are available at https://doi.org/10.1038/s41586-024-07712-6.

1. Li, L. et al. Flexible all-perovskite tandem solar cells approaching 25% efficiency with molecule-bridged hole-selective contact. *Nat. Energy* **7**, 708–717 (2022).
2. Tan, Q. et al. Inverted perovskite solar cells using dimethylacridine-based dopants. *Nature* **620**, 545–551 (2023).
3. He, R. et al. Improving interface quality for 1-cm^2 all-perovskite tandem solar cells. *Nature* **618**, 80–86 (2023).
4. Al-Ashouri, A. et al. Conformal monolayer contacts with lossless interfaces for perovskite single junction and monolithic tandem solar cells. *Energy Environ. Sci.* **12**, 3356–3369 (2019).
5. Zhang, S. et al. Minimizing buried interfacial defects for efficient inverted perovskite solar cells. *Science* **380**, 404–409 (2023).
6. Wang, S. et al. Advantages and challenges of self-assembled monolayer as a hole-selective contact for perovskite solar cells. *Mater. Futures* **2**, 012105 (2023).
7. Borissov, A. et al. Recent advances in heterocyclic nanographenes and other polycyclic heteroaromatic compounds. *Chem. Rev.* **122**, 565–788 (2022).
8. Zhang, Y. et al. Recent advances in n-type and ambipolar organic semiconductors and their multi-functional applications. *Chem. Soc. Rev.* **52**, 1331–1381 (2023).
9. Peng, X. et al. Recent progress in cyclic aryliodonium chemistry: syntheses and applications. *Chem. Rev.* **123**, 1364–1416 (2023).
10. Al-Ashouri, A. et al. Monolithic perovskite/silicon tandem solar cell with >29% efficiency by enhanced hole extraction. *Science* **370**, 1300–1309 (2020).
11. Ullah, A. et al. Versatile hole selective molecules containing a series of heteroatoms as self-assembled monolayers for efficient p–i–n perovskite and organic solar cells. *Adv. Funct. Mater.* **32**, 2208793 (2022).
12. Truong, M. A. et al. Tripodal triazatruxene derivative as a face-on oriented hole-collecting monolayer for efficient and stable inverted perovskite solar cells. *J. Am. Chem. Soc.* **145**, 7528–7539 (2023).
13. Ullah, A. et al. Novel phenothiazine-based self-assembled monolayer as a hole selective contact for highly efficient and stable p–i–n perovskite solar cells. *Adv. Energy Mater.* **12**, 2103175 (2022).
14. Zhang, G. et al. Renewed prospects for organic photovoltaics. *Chem. Rev.* **122**, 14180–14274 (2022).
15. Li, C. et al. Rational design of Lewis base molecules for stable and efficient inverted perovskite solar cells. *Science* **379**, 690–694 (2023).
16. Li, Z. et al. Organometallic-functionalized interfaces for highly efficient inverted perovskite solar cells. *Science* **376**, 416–420 (2022).
17. Li, X. et al. Constructing heterojunctions by surface sulfidation for efficient inverted perovskite solar cells. *Science* **375**, 434–437 (2022).
18. Li, F. et al. Hydrogen-bond-bridged intermediate for perovskite solar cells with enhanced efficiency and stability. *Nat. Photon.* **17**, 478–484 (2023).
19. Jiang, Q. et al. Surface reaction for efficient and stable inverted perovskite solar cells. *Nature* **611**, 278–283 (2022).
20. Zhu, J. et al. A donor–acceptor-type hole-selective contact reducing non-radiative recombination losses in both subcells towards efficient all-perovskite tandems. *Nat. Energy* **8**, 714–724 (2023).
21. Li, L. et al. Self-assembled naphthalimide derivatives as an efficient and low-cost electron extraction layer for n–i–p perovskite solar cells. *Chem. Commun.* **55**, 13239–13242 (2019).
22. Li, E. et al. Bonding strength regulates anchoring-based self-assembly monolayers for efficient and stable perovskite solar cells. *Adv. Funct. Mater.* **31**, 2103847 (2021).
23. Zheng, X. et al. Co-deposition of hole-selective contact and absorber for improving the processability of perovskite solar cells. *Nat. Energy* **8**, 462–472 (2023).
24. Zhang, S. et al. Conjugated self-assembled monolayer as stable hole-selective contact for inverted perovskite solar cells. *ACS Mater. Lett.* **4**, 1976–1983 (2022).
25. Briou, B. et al. Trends in the Diels–Alder reaction in polymer chemistry. *Chem. Soc. Rev.* **50**, 11055–11097 (2021).
26. Blade, H. et al. Conformations in solution and in solid-state polymorphs: correlating experimental and calculated nuclear magnetic resonance chemical shifts for tolfenamic acid. *J. Phys. Chem. A* **124**, 8959–8977 (2020).
27. Bujosa, S. et al. Self-assembly of amphiphilic aryl-squaramides in water driven by dipolar π–π interactions. *Org. Biomol. Chem.* **18**, 888–894 (2020).
28. Yao, C. et al. Reversible sol–gel transition of oligo(*p*-phenylenevinylene)s by π–π stacking and dissociation. *J. Phys. Chem. B* **118**, 4661–4668 (2014).
29. Allix, F. et al. Evidence of intercolumnar π–π stacking interactions in amino-acid-based low-molecular-weight organogels. *Langmuir* **26**, 16818–16827 (2010).
30. Wang, C. et al. Temperature-dependent Raman study and molecular motion in L-alanine single crystal. *J. Chem. Phys.* **55**, 3291–3299 (2003).
31. McGrane, S. D. et al. Anharmonic vibrational properties of explosives from temperature-dependent Raman. *J. Phys. Chem. A* **109**, 9919–9927 (2005).
32. Kumar, J. et al. Breathing mode's temperature coefficient estimation and interlayer phonon scattering model of few-layer phosphorene. *ACS Omega* **7**, 43462–43467 (2022).

Methods

Materials

The transparent ITO glass (10 Ω per square, transmittance 88%) was purchased from Shenzhen Huayu United Technology. The perovskite raw materials, including lead iodide (PbI_2, purity 99.999%), formamidinium iodide (FAI, purity 99.99%), methylammonium bromide (MABr, purity 99.9%), methylammonium chloride (MACl, purity 99.9%), lithium fluoride (LiF, purity 99.99%) and C_{60} (purity 99.9%) were all purchased from Advanced Election Technology. Bathocuproine (purity 99%), caesium iodide (CsI, purity 99.999%) and oleylammonium iodide (OAmI, purity 99.5%) were purchased from Xi'an Polymer Light Technology. 2PACz (purity 98%) was obtained from Tokyo Chemical Industry. The required solvents, including *N*,*N*-DMF (extra dry, purity 99.8%), isopropanol (IPA, extra dry, purity 99.8%), ethanol (extra dry, purity 99.8%) and ethyl acetate (extra dry, purity 99.5%) were purchased from J&K Scientific. Dimethyl sulfoxide (DMSO, anhydrous, ≥99.9%) and silver (purity 99.99%) was purchased from Sigma-Aldrich. All chemical reagents were used as received without further purification unless otherwise specified.

Preparation of perovskite films

For the preparation of perovskite films with a composition of $(FA_{0.98}MA_{0.02})_{0.95}Cs_{0.05}Pb(I_{0.98}Br_{0.02})_3$, 1.65-M perovskite precursor solution was prepared by dissolving CsI, FAI, MABr, $PbBr_2$ and PbI_2 in 1 ml mixed solvent of DMF and DMSO at a volume ratio of 4:1. Additional 7 mol% PbI_2 and 15 mol% MACl was added to the precursor solution and the solution was stirred overnight. The filtered perovskite precursor was then spin-coated on substrate at 1,000 rpm for 10 s and 5,000 rpm for 40 s in a nitrogen glovebox. During the second spinning step, 250 µl of ethyl acetate anti-solvent was dropped quickly at 25 s. Afterwards, the film was annealed at 110 °C for 20 min.

For preparation of wide-bandgap perovskite films with a composition of $Cs_{0.05}MA_{0.15}FA_{0.8}PbI_{2.25}Br_{0.75}$, 1.65-M perovskite precursor solution was prepared by dissolving CsI, MABr, FAI, $PbBr_2$ and PbI_2 in 1 ml mixed solvent of DMF and DMSO at a volume ratio of 4:1. Additional 5 mol% PbI_2 and 10 mol% MACl was added to the precursor solution and the solution was stirred overnight. The filtered perovskite precursor was then spin-coated on substrate at 1,000 rpm for 10 s and 5,000 rpm for 40 s in a nitrogen glovebox. During the second spinning step, 250 µl of ethyl acetate anti-solvent was dropped quickly at 25 s. Afterwards, the film was annealed at 100 °C for 30 min.

For the preparation of narrow-bandgap perovskite films with a composition of $FAPbI_3$, 1.5-M perovskite precursor solution was prepared by dissolving FAI and PbI_2 in 1 ml mixed solvent of DMF and DMSO at a volume ratio of 4:1. Then 20 mol% of MACl was added to the perovskite precursor solution and stirred for 2 h. The filtered perovskite precursor was spin-coated on substrate at 1,000 rpm for 3 s and 4,000 rpm for 60 s in a nitrogen glovebox, and 300 µl of ethyl acetate anti-solvent was dropped quickly at 20 s during the second spinning step. Then these films were annealed at 90 °C for 1 min and 150 °C for 25 min, respectively.

Fabrication of inverted PSC devices

First, the ITO glass (15 mm × 15 mm) was washed with detergent solution, acetone and absolute ethanol under sonication for 30 min each followed by drying with a pure nitrogen flow. The cleaned and dry ITO substrates were then treated with ultraviolet ozone for 25 min, and then transferred into a glovebox filled with nitrogen. To deposit the 2PACz (or MeO-2PACz or Me-4PACz) or Py3 layer on the ITO glass, the molecule solution with 0.6 mg ml^{-1} (0.2, 0.4, 0.8, 1.0 and 1.2 mg ml^{-1} for fabrication of molecular films with different thicknesses) in mixed solvent of ethanol and DMF at a volume ratio of 3:1 was spin-coated at 1,000 rpm for 10 s and 3,000 rpm for 40 s in a nitrogen glovebox. The role of adding DMF as a co-solvent is to improve the dispersion of the molecules in the solvent. Afterwards, the film was annealed at 130 °C for 20 min. After cooling to room temperature, the perovskite films were coated on the 2PACz or Py3 layer following the abovementioned method. For the surface passivation layer, the OAmI was dissolved in isopropanol with a concentration of 1 mg ml^{-1} and stirred at room temperature (20–25 °C) for 2 h. Then 60 µl of OAmI solution was spin-coated on top of the as-prepared perovskite at 5,000 rpm for 40 s, and then transferred to the hotplate and annealed at 100 °C for 1 min. The above spin-coating processes were all conducted at room temperature (20–25 °C) in nitrogen.

After cooling to room temperature, the whole device was transferred to a vacuum chamber under a base pressure of $<5.0 \times 10^{-6}$ Pa. Then 0.7 nm LiF at a rate of 0.1 Å s^{-1}, 40 nm C_{60} at a rate of 0.2 Å s^{-1} and 6 nm BCP at a rate of 0.2 Å s^{-1} were thermally evaporated on the perovskite thin film sequentially (Angstrom Engineering) without breaking vacuum. Finally, 120-nm-thick silver electrode at a rate of 1.5 Å s^{-1} was deposited to complete the devices for *J*–*V* measurements or stability tests. Approximately 120-nm MgF_2 was also evaporated at the glass side to minimize the reflection losses from the glass substrates.

Device stability tests

The devices for stability tests were fabricated using the method described above with a structure of ITO/2PACz or Py3/perovskite/C_{60}/BCP/Ag. The thickness of the C_{60} layer was 100 nm. A thicker C_{60} layer was used to serve as an internal encapsulation of its underlying perovskite layer. Owing to the hydrophobicity of C_{60}, the perovskite layer can be protected from moisture, and thus the device degradation can be mitigated. The ITO glass (15 mm × 15 mm) was etched in half by a laser. A piece of device contained four subcells. The devices were encapsulated by a glass–glass encapsulation technology combined with an edge seal (UV Curing Sealant, three-bond 3035B) to seal the device under ultraviolet-light illumination (light-emitting diode (LED) flood lamp, DELOLUX 20) in a nitrogen-filled glovebox. A piece of black tape was attached to the exterior of the cover glass to protect the solar cell during ultraviolet curing. Indium solar ribbon was used to protect the evaporated metal electrode of the solar cells.

To evaluate the device stability following the ISOS-L-1 protocol, we stored the devices in the test chamber as shown in Supplementary Fig. 13a. The PCE of the encapsulated devices were tracked under continuous AM 1.5G illumination (100 mW cm^{-2}, white LED) in ambient air at about 35 °C. The thermal stability test of the device following the ISOS-D-2 protocol was conducted in the dark and a nitrogen atmosphere with continuous heating of the unencapsulated device at about 85 °C. The PCE of the devices was tracked over time and the *J*–*V* measurements were performed after cooling the devices to room temperature. The light-heat stability test following the ISOS-L-2 protocol was conducted in a nitrogen atmosphere with continuous heating at about 65 °C and under continuous AM 1.5G illumination of the unencapsulated device. The PCE of the devices was tracked over time and the *J*–*V* measurements were performed after cooling the devices to room temperature. The maximum-power-point tracking of the devices was conducted under AM 1.5 G illumination (100 mW cm^{-2}) in ambient air at about 35 °C and about 55 °C. The devices were stored in the test chamber as shown in Supplementary Fig. 13b. The voltage at the maximum power point was automatically adjusted and applied, and the power output of the devices was tracked over time.

Device characterization

The *J*–*V* characteristics of photovoltaic cells were measured using a Keithley 2400 source measure unit under a simulated AM 1.5G spectrum, with an Oriel 9600 solar simulator. The illumination light was calibrated to 100 mW cm^{-2} AM 1.5G using a silicon reference cell. Typically, the devices were measured in reverse scan (1.20 V → 0 V, step 0.02 V).

All the devices were measured without pre-conditioning such as light soaking and applied a bias voltage. Steady-state PCE was calculated by measuring stabilized photocurrent density under a constant bias voltage. For the dark *J*–*V* measurements, the shutter was closed and the devices were scanned from −0.1 V to 1.2 V with a step of 0.02 V. For the measurements of the ideality factor, the light intensity was varied and the corresponding open-circuit voltages were derived from the measured *J*–*V* curves. External quantum efficiencies were measured using an integrated system (Enlitech) and a lock-in amplifier with a current preamplifier under short-circuit conditions. Transient photovoltage decay under open-circuit conditions and transient photocurrent decay under short-circuit conditions were conducted using a photo-electrochemical measurement system. The high-angle annular dark-field images and energy dispersive X-ray mapping of the cross-sectional devices were investigated with a field-emission scanning electron microscope (Talos F200X G2, Thermo Fisher Scientific) equipped with an energy dispersive X-ray and a high-angle annular dark-field detector in STEM mode at 200-kV operating voltage. Sample preparation involved creating a cross-sectional lamella in a scanning electron microscope (Helios 5 UX, Thermo Fisher Scientific) with an EasyLift nanomanipulator, aided by a gallium-focused ion beam. Protective carbon and platinum layers were deposited on the sample using electron and ion beams to prevent damage.

Materials characterization

All the samples were prepared in a nitrogen glovebox and transferred into a container filled with nitrogen before sending out for different characterizations.

For the AFM and c-AFM measurements of the molecular films, the 2PACz and Py3 films were prepared in a nitrogen glovebox by spin-coating the 2PACz and Py3 precursor solutions (0.6 mg ml^{-1} in mixed solvent of ethanol and DMF at a volume ratio of 3:1) at 1,000 rpm for 10 s and subsequently 3,000 rpm for 40 s, followed by annealing at 130 °C for 20 min. The samples were then transferred into a container filled with nitrogen after cooling to room temperature. The as-prepared samples were subsequently sent out for the AFM and c-AFM measurements using the Cypher ES Oxford Instruments at a bias of 500 mV. For the XRD measurements, to assess the perovskite films deposited on top of the molecular layers, the perovskite layers were prepared following the method described above, and the measurements were performed on sealed-tube copper X-ray source, equipped with a 1D LynxEye detector. For the measurements of the molecular films, the 2PACz and Py3 films were prepared by drop-casting the 2PACz and Py3 precursor solutions to make thicker films for better signals. The samples then underwent different stability tests before the tests, and the instrument used was the same as for the measurement of the perovskite films. Kelvin probe force microscopy was conducted by Environmental Atomic Force Microscopy (Cypher ES).

In the NMR measurements for the stability tests, the samples were stored in a vial that was transferred from ambient atmosphere to a glovebox for the ageing test. The samples were aged under continuous illumination using a xenon lamp in a nitrogen glovebox at ambient temperature. Owing to the heating effect of light, the real temperature was detected to be around 45 °C via a thermometer. The NMR spectra were measured by a 500-MHz solution NMR spectrometer with a room-temperature probe (Bruker Biospin). The ssNMR spectroscopy was recorded on a Bruker 500-MHz widebore magnet spectrometer equipped with AVANCE NEO console and 3.2-mm HXY magic-angle-spinning probe configured in double-resonance mode. Variable-temperature proton NMR spectra were collected with a recycle delay of 2 s, varied at an interval of 10 °C ranging from 0 °C to 80 °C, and stabilized for 15 min at each temperature point before recording. All experiments were measured at a magic-angle-spinning frequency of 20 kHz by using the homonuclear decoupling scheme phase-modulated Lee–Goldburg for enhanced spectral resolution. All spectra were processed with the same window function parameters in Bruker Topspin for quantitative comparison, and referenced to the proton chemical shift of tetramethylsilane at 0 ppm. Simulations and analyses of proton NMR spectra were performed in the solid lineshape analysis module included in the Topspin 4.0 software.

For the Raman and FTIR spectroscopy, the 2PACz and Py3 powders were stored in brown vials filled with nitrogen before being sent out for measurements. The temperature-dependent Raman measurement was realized on alpha 300R (WITec) confocal Raman system combining a Linkam THMS600 stage. A diode-pumped solid-state laser (785 nm, cobalt laser) was focused on the sample with a diffraction-limited beam size of 900 nm by a long-working-distance ×50 objective (numerical aperture 0.55). To get a better spectral signal-to-noise ratio, the laser power was set to 40 mW and the integration time of collecting spectrum was set to 40 s. The Linkam THMS600 stage was used to adjust and guarantee the accuracy of temperature. It is important to keep the preset temperature for at least 15 min before each measurement. For the polarized FTIR measurements, 30-nm ITO was first deposited on 2-mm-thick Al_2O_3 substrates with d.c. magnetron sputter deposition at room temperature. To deposit the 2PACz or Py3 layer on the Al_2O_3/ITO substrates, the 2PACz or Py3 solution with 0.6 mg ml^{-1} in mixed solvent of ethanol and DMF at a volume ratio of 3:1 was spin-coated at 1,000 rpm for 10 s and 3,000 rpm for 40 s in a nitrogen glovebox. Afterwards, the film was annealed at 130 °C for 20 min as fresh sample. For the assessment of the aged samples, the fresh films were further heated at 130 °C for 10 min or 20 min before measurements. The polarized FTIR spectra were captured at room temperature with an FTIR spectrometer (Thermo Fisher Nicolet IS50) equipped with a DTGS KBr detector. The polarizer is made of ZnSe, which limits the low-end spectral range to around 650 cm^{-1}. In these experiments, a unique background is required for each polarization position used. For example, if you are going to collect spectra at 0° and 90°, corresponding background spectra are required at 0° and 90°. The spectral resolution was set to 4 cm^{-1}, the aperture was set to 4 mm and spectra were acquired by averaging 256 scans.

For the high-resolution X-ray photoelectron spectroscopy (XPS) measurements, the 2PACz and Py3 films were prepared using the same method as for the AFM measurements. The samples were then loaded into the XPS instrument (Thermo Fisher ESCALAB Xi+) and an Al Kα (1486.6 eV) X-ray was used as the excitation source. The ultraviolet photoelectron spectroscopy measurements were performed using the same samples of 2PACz and Py3 films as XPS. A helium discharge lamp, emitting ultraviolet energy at 21.22 eV, was used for excitation. All ultraviolet photoelectron spectroscopy measurements were performed using standard procedures with a −10-V bias applied between the samples and detectors. Clean gold was used as a reference. Ultraviolet–visible absorption spectra of the different molecule samples, the perovskite films and the bare ITO glass were obtained using a Shimadzu UV-VIS-NIR (UV3600Plus + UV2700) equipped with integrating sphere, in which monochromatic light was incident to the substrate side for the film samples.

For the time-resolved photoluminescence (TRPL) spectroscopy measurements, the sample was excited with a picosecond pulsed diode laser (Pico-quant LDH 450), with a 70-ps pulse width and 20-MHz repetition rate, focused on sample with a ×100 objective (numerical aperture 0.90). The photoluminescence signal was acquired through the TCSPC strobelock system. The energy density of laser for TRPL measurements was set to be 2.6 nJ cm^{-2} and 26.2 nJ cm^{-2}, respectively. The total instrument response function for the photoluminescence decay was less than 200 ps and the temporal resolution was less than 30 ps. The contact-angle measurements of the 2PACz- or Py3-layer-covered ITO substrates were recorded in a range of 0–180° with high precision (±0.1° accuracy) using an OCA25 contact-angle analyser. Scanning electron microscopy was carried out on the Field Emission Environment Scanning Electron Microscope of QuattroS.

We used ultra-performance liquid chromatography to semi-quantify the density of the molecules in the as-deposited films of Py3 and 2PACz. First, the ITO glass (15 mm × 15 mm) was washed with detergent solution, acetone and absolute ethanol under sonication of 30 min each followed by drying with a pure nitrogen flow. The cleaned and dry ITO substrates were then treated with ultraviolet ozone for 25 min, and then transferred into a glovebox filled with nitrogen. To deposit the 2PACz layer or the Py3 layer on ITO glass, the 2PACz or Py3 solution with 0.6 mg ml^{-1} in mixed solvent of ethanol and DMF at a volume ratio of 3:1 was spin-coated at 1,000 rpm for 10 s and 3,000 rpm for 40 s in a nitrogen glovebox. For each case, we placed 40 substrates into a 50-ml brown vial and added 30 ml methanol. The molecules were removed from the ITO substrates by ultrasonic exfoliation and dissolved in menthol for the ultra-performance liquid chromatography measurements. The density of the molecules on each substrate was determined by the total molecular concentration divided by the area of the substrate and the number of substrates used. The instrument we used (ACQUITY UPLC, H-Class, Waters) was coupled with photodiode array detector with a BEH C18 column (1.7 µm, 2.1 mm × 50 mm, Waters). The mobile phase A was water solution (0.1% formic acid, v/v) and the mobile phase B was acetonitrile. The initial mobile phase was 20% B, increasing to 80% B in 2 min and maintaining for 2 min later. The post running time was 2.0 min. The elution was performed at 40 °C with flow rate of 0.4 ml min^{-1}. Two single photodiode array detector channels at 260 nm and 275 nm were used for 2PACz and Py3, and the retention time was 1.65 min and 1.94 min, respectively. All data were collected and processed with Empower 3 software.

Data availability

All the data needed to evaluate the conclusions in the paper are present in the paper or Supplementary Information.

Acknowledgements We thank L. Liu, X. Miao and T. Zhou from the Instrumentation and Service Center for Physical Sciences (ISCPS) and X. Lu, Y. Chen, Z. Chen, Y. Cheng and C. Wang from the Instrumentation and Service Center for Molecular Sciences at Westlake University for assistance with the characterizations. J. Xue and R.W. acknowledge grants (grant numbers LR24F040001, LD22E020002 and LD24E020001) from the Natural Science Foundation of Zhejiang Province of China. J. Xue acknowledges grants from the National Natural Science Foundation of China (grant number 62274146), and the financial support by Shanxi-Zheda Institute of Advanced Materials and Chemical Engineering (grant number 2021SZ-FR006). R.W. acknowledges the support of Key R&D Program of Zhejiang (2024SSYS0061). H.-f.W. acknowledges the National Key Instrumentation Development grant by the National Natural Science Foundation of China (grant number 21727802). This work was also supported by the Fundamental Research Funds for the Central Universities (226-2022-00200).

Author contributions J. Xue, R.W., Q.L. and K.Z. conceived the idea. Q.L. synthesized Py3. K.Z. and L.Y. fabricated the perovskite films and devices. K.Z. and Q.L. did the data analysis under the supervision of R.W. and J. Xue. C.D. and I.Y. conducted the theoretical calculations. C.D., J.S., X.Z., P.S., Y.T., Y.L., J. Xu, J.Z., D.J., S.W., W.F., S.Z., S.C., X.W. and L.T. assisted with the characterizations and device fabrication. L.Z. performed the sum-frequency generation measurements under the supervision of H.-f.W. R.L. and D.Y. provided helpful discussions. J. Xue wrote the paper. All authors discussed the results and commented on the paper.

Competing interests The authors declare no competing interests.

Additional information
Supplementary information The online version contains supplementary material available at https://doi.org/10.1038/s41586-024-07712-6.
Correspondence and requests for materials should be addressed to Rui Wang or Jingjing Xue.
Peer review information *Nature* thanks Jun Yin, Yu-Wu Zhong and the other, anonymous, reviewer(s) for their contribution to the peer review of this work.
Reprints and permissions information is available at http://www.nature.com/reprints.

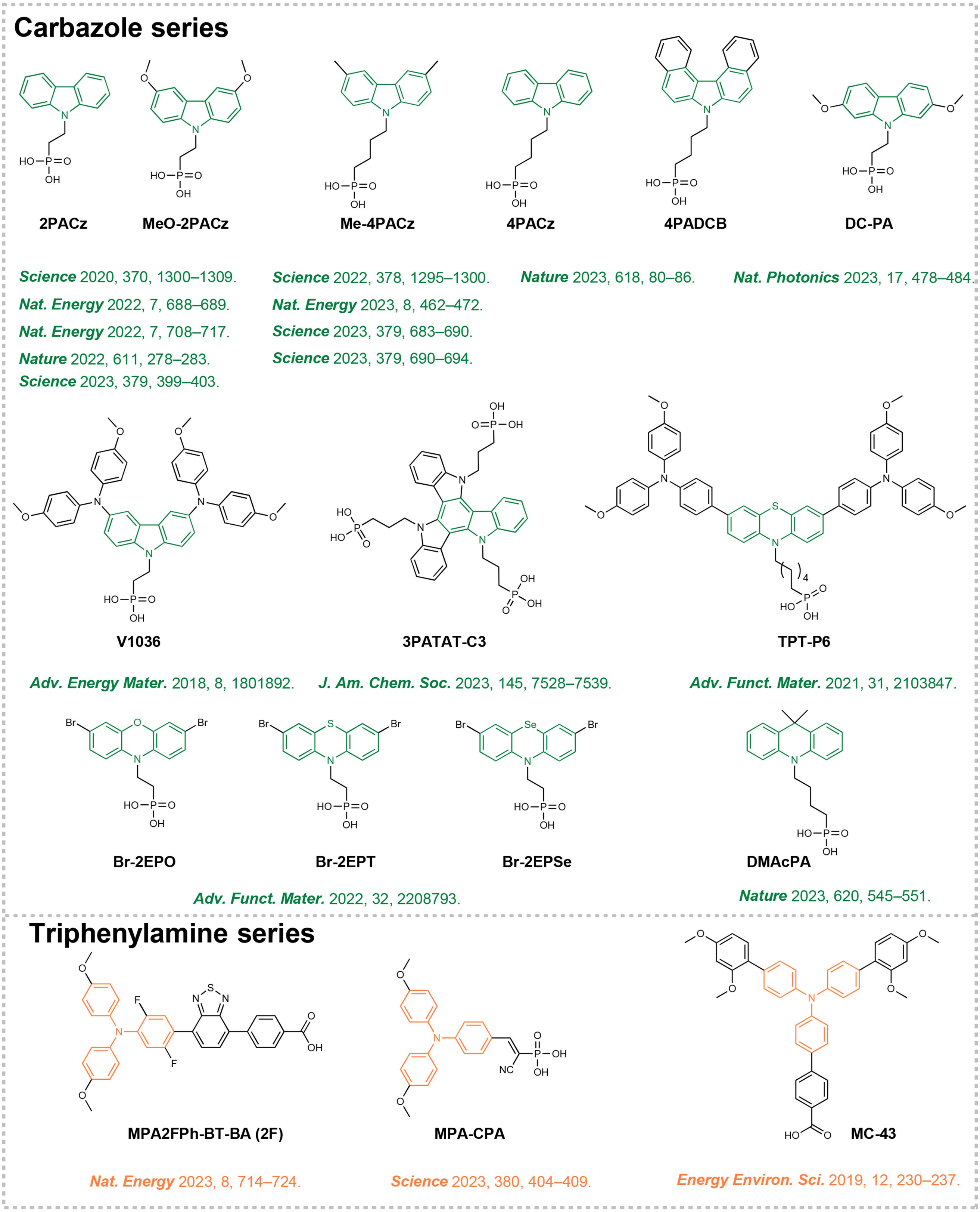

Extended Data Fig. 1 | A summary of the molecules reported for making hole selective contacts. Chemical structures of reported molecule-based hole selective contacts in PSCs.

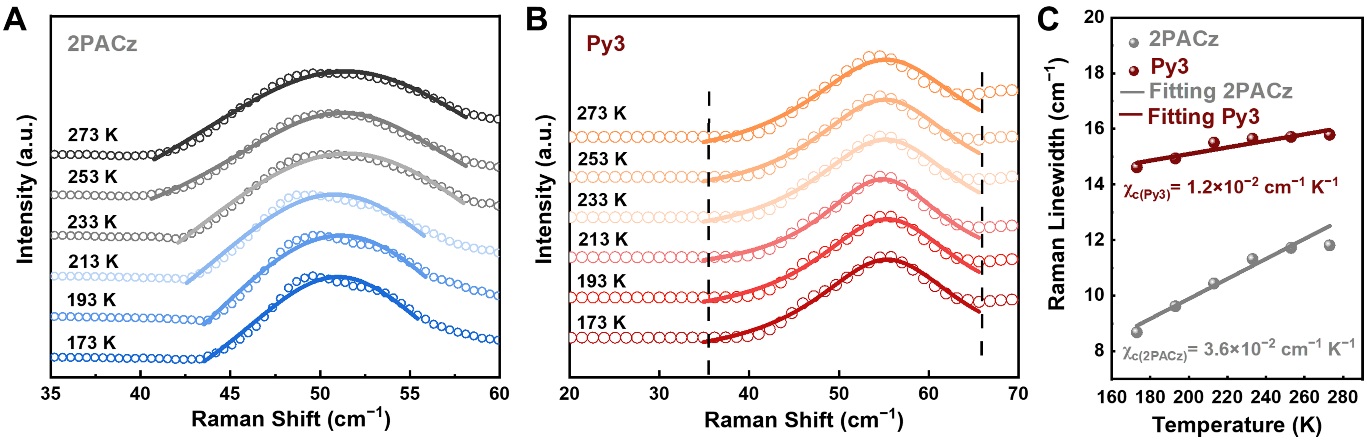

Extended Data Fig. 2 | Temperature-dependent Raman spectra of the assembled molecules. Temperature-dependent Raman spectra at the low-frequency phonon region of (**A**) 2PACz and (**B**) Py3. (**C**) The change of Raman linewidth as a function of temperature for 2PACz and Py3.

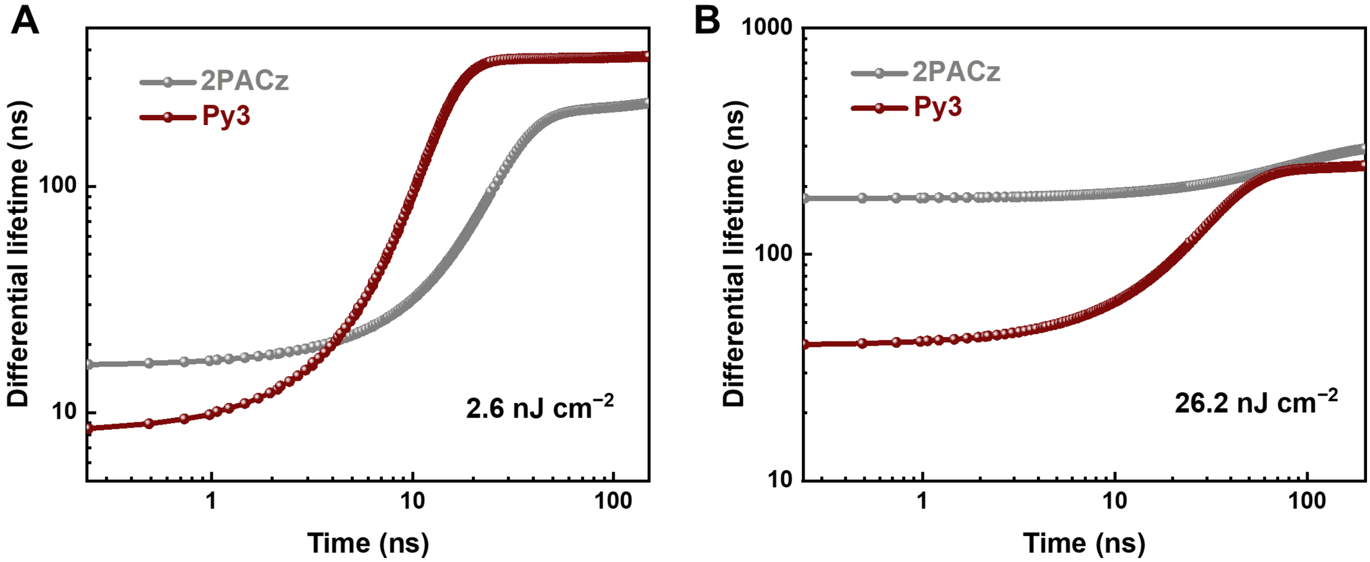

Extended Data Fig. 3 | TRPL measurements of the molecular films deposited on the ITO substrates. Differential lifetime $\tau_{PL}(t)$ derived from TRPL measurements at different laser fluences for 2PACz (A) and Py3 (B). The first interval at short times is dominated by the charge transfer, and the second interval at longer times is governed by carrier recombination. For higher laser fluences the two lifetimes are less easy to distinguish due to stronger charge accumulation at the interface. At both relatively low and higher laser fluence.

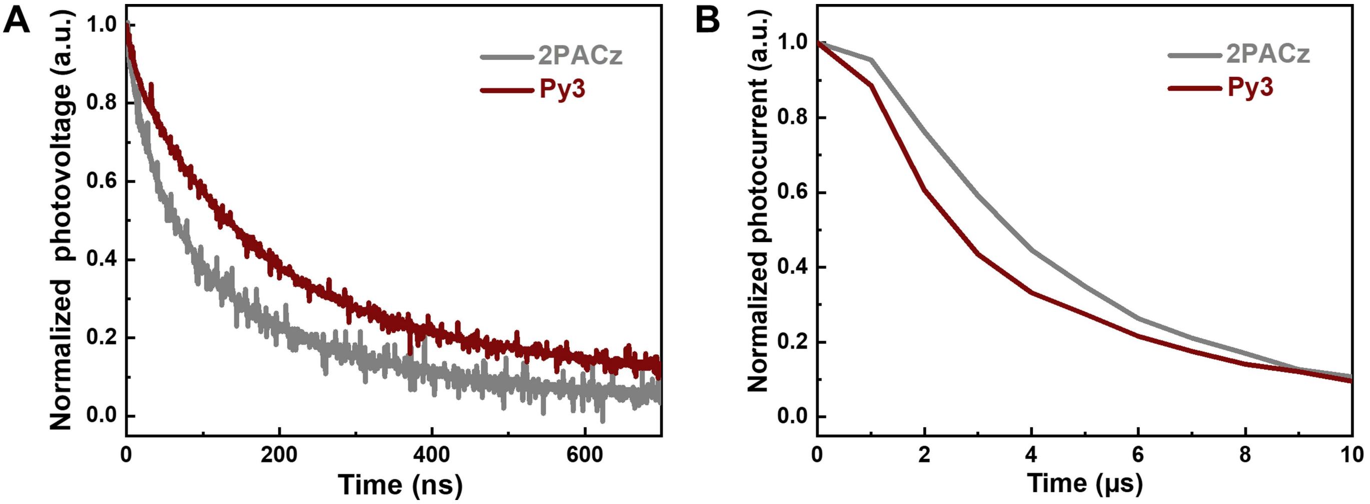

Extended Data Fig. 4 | TPV and TPC measurements of the solar cells. (**A**) TPV under the open-circuit condition and (**B**) TPC under the short-circuit condition for 2PACz and Py3-based PSCs.

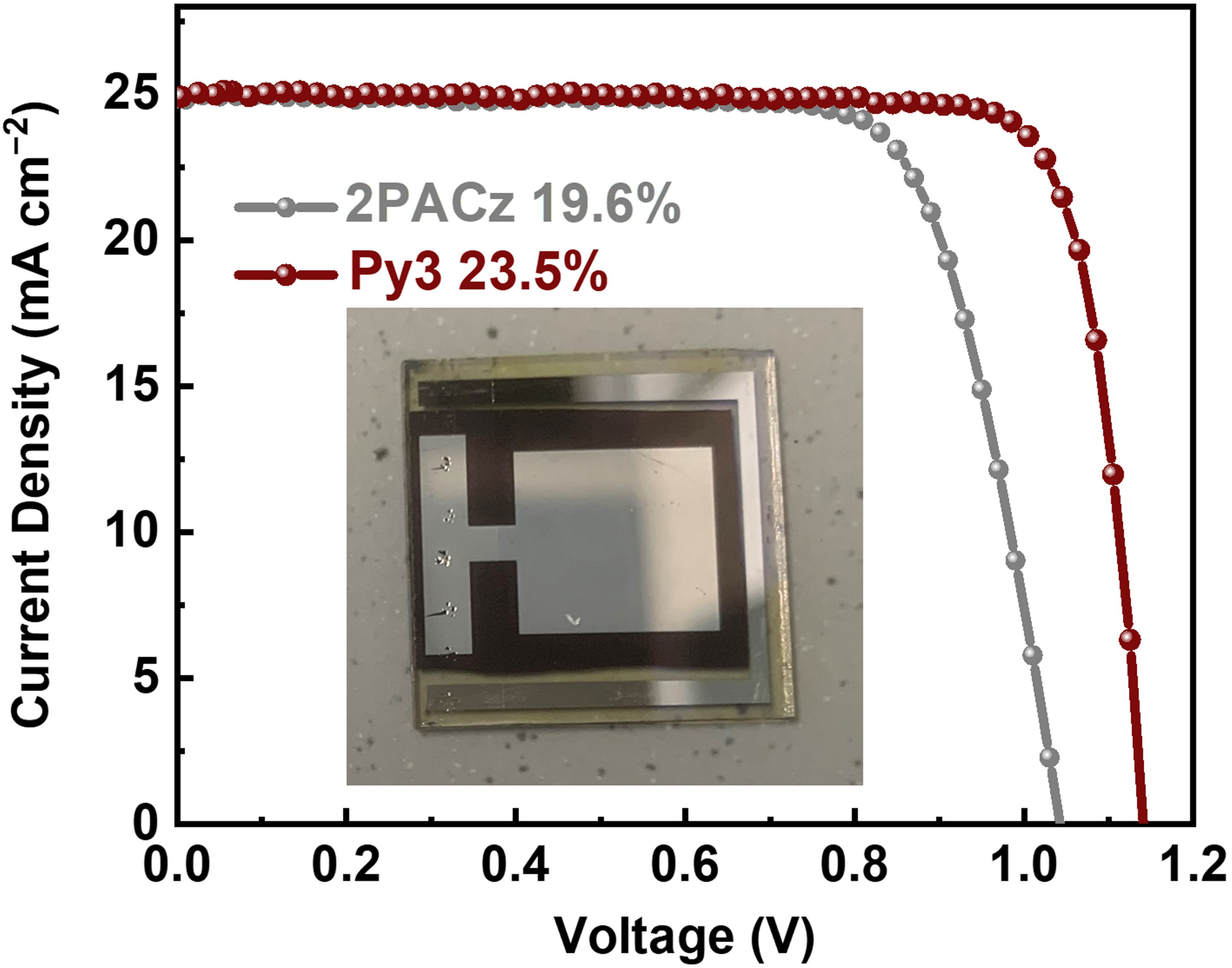

Extended Data Fig. 5 | Upscaling of the solar cell devices. *J-V* curves of champion scaled-up PSCs based on 2PACz and Py3. (Inset) Photograph of the 1-cm^2 cell.

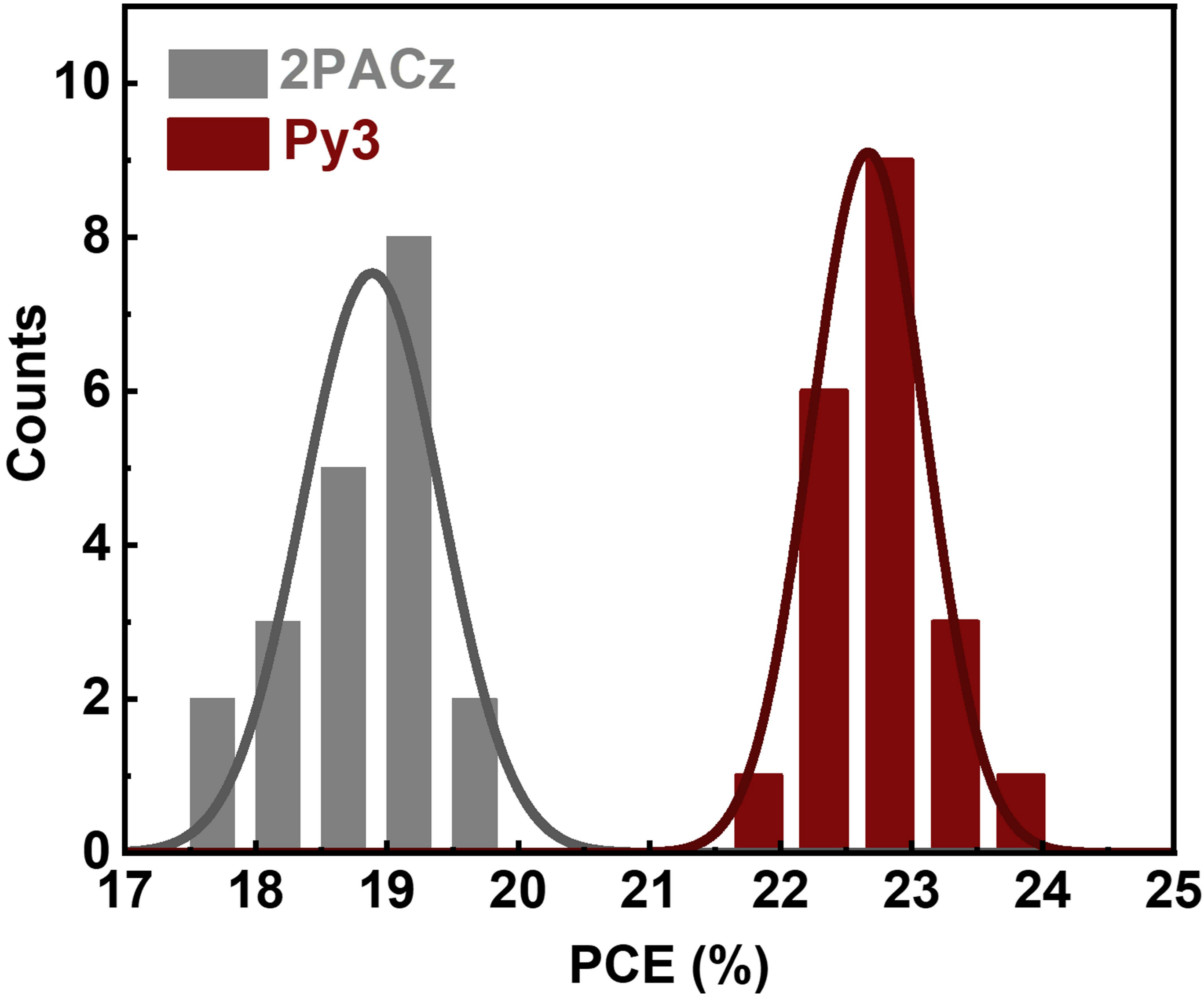

Extended Data Fig. 6 | Statistical results of the device performance. The statistics of PCE values for scaled-up PSCs based on 2PACz and Py3. Histograms showing the device efficiencies of 20 cells per type, fitted with Gaussian distributions (solid lines).